Effect of ZnS and PbS shell on mem-behavior of CdS quantum dots

Hirendra Das[1,*] ⓘ, Qiang Xu[2], and Pranayee Datta[1]

[1] *Department of Electronics and Communication Technology, Gauhati University, Assam, India*
[2] *Department of Mechanical Engineering, University of Huddersfield, Huddersfield, UK*

ABSTRACT

In this paper, a systematic study is carried out on mem-behavior of CdS, CdS@ZnS, and CdS@PbS core–shell nanocomposites with emphasis on the effect of ZnS and PbS shell on mem-behavior of CdS quantum dots. From X-ray diffraction, the CdS quantum dots are found to be hexagonal in nature with average crystallite size ∼ 10.3 nm. From high-resolution transmission electron microscope images, the particle size is calculated around 3–4 nm for CdS quantum dots. For core–shell nanoparticles, formation of epitaxial shell layer on CdS core is clearly evident with enhancement in particle sizes. Active layer of as-synthesized samples is deposited on Indium tin oxide-coated glass which is used as one electrode. Aluminium is used as counter electrode and deposited over the active layer using thermal evaporation technique. The fabricated devices show bipolar switching characteristics with prominent hysteresis loops. The current–voltage characteristics of the devices show memristive, memcapacitive, and meminductive behavior depending on the type of active layer used. It is also observed that the inclusion of ZnS and PbS shell significantly alters the mem-behavior of the CdS quantum dots which is the major finding of this study. The conduction through the device is found to be due to coulomb blockade which also supports the ON/OFF switching mechanism. The sensitivity of the devices can be determined from R_{ON}/R_{OFF} ratio, and it is found to be higher for CdS@ZnS core–shell nanoparticles compared to CdS quantum dots and CdS@PbS nanoparticles.

Abbreviations

CdS	Cadmium sulphide
ZnS	Zinc sulphide
PbS	Lead sulphide
ZnO	Zinc oxide
CdSe	Cadmium selenide
Fe_2O_3	Ferric oxide
R	Resistor
L	Inductor
C	Capacitor

Address correspondence to E-mail: hirendra.das100@gmail.com

Ⓢ Springer

PVA	Polyvinyl alcohol
q	Charge
Φ	Magnetic flux
Cu	Copper
ITO	Indium tin oxide
Al	Aluminium
PVP	Polyvinylpyrrolidone
QDs	Quantum dots
XRD	X-ray diffraction
UV–Vis	Ultra violet–visible spectroscopy
PL	Photoluminescence spectroscopy
FWHM	Full width at half maximum
HRTEM	High-resolution transmission electron microscopy
SAED	Selected area electron diffraction
EDS	Energy-dispersive X-ray spectroscopy
AFM	Atomic force microscopy
MR	Memristive
MC	Memcapacitive
MI	Meminductive
MEF	Memristor efficiency factor
HRS	High resistance region
LRS	Low resistance region
HWO	Hysteresis width at '0V'
CB	Coulomb blockade
RT	Resonant tunneling
NDR	Negative differential resistance

1 Introduction

There are three fundamental passive circuit elements, namely, resistor (R), capacitor (C), and inductors (L), which are used as building blocks for electronic circuits. Their behavior can be described by the relations between the variables: current, voltage, charge, and magnetic flux. However, in 1971, Leon Chua [1] proposed a fourth circuit element relating the electric charge (q) and the magnetic flux Φ_m using the relation $M(q) = \dfrac{\mathrm{d}\Phi_m}{\mathrm{d}q}$ where $M(q)$ is memristance. In 2008, Strukov et al. [2] reported a physical model of two terminal electrical device which acts like a perfect memristor for a certain range of w, where w is the state variable of the device related to the width of the channel region. Strukov also demonstrated that in nanoscale systems, memristance arises naturally where coupling of electronic and ionic transport

occurs under the influence of an external bias. In the past few decades, nanomaterials have attracted enormous attention of the researchers in different field of science and technology due to their unique size dependent structural, optical, and electronic properties [3–5]. In nanocrystals/quantum dots having interface traps, hysteresis type dependence of capacitance C on the applied voltage is observed [6, 7]. Quantum dots/nanocomposites exhibit memcapacitive (MC) and meminductive (MI) behavior due to their inductive and capacitive properties [8]. Kim et al. [9] in 2009 investigated the electrical conductivity of nanoparticle assemblies consisting of an infinite number of monodispersed crystalline magnetite (Fe_2O_3) particles and found that assembly of nanoparticles having sizes below 10 nm at room temperature exhibits a voltage–current (V–I) hysteresis with an abrupt enlarge bipolar resistance switching properties. Experimental works on memristive properties of ZnS/PVA and ZnO/PVA nanocomposites were reported by Bhadra et al. [10] which supports the observations of Kim's group. Sarma et al. [11] reported study of memristive, memcapacitive, and meminductive properties of undoped and copper (Cu)-doped CdS quantum dots embedded in polyvinyl alcohol (PVA). Cheng et al. [12] reported memristive properties of 1 T phase MoS_2 nanosheets based on voltage-dependent change in resistance. Memristive effect on Au/CZTE core–shell nanoparticles were reported by Chakrabarti et al. in 2015 [13] where they explained the memristive effect of nanostructures from its density of state. Transient metal ions are used with ZnO quantum dots to increase the R_{ON}/R_{OFF} ratio for ultrafast programmable devices by Yang et al. [14] and it was further developed by Younis et al. [15] with ZnO nanorod devices. Simulation works on memristive devices for memory application using CdSe and CdS quantum dots were reported by Devi et al. [16] in 2018 where it was explained that the R_{ON}/R_{OFF} ratio of the memristor depends on the time-dependent resistance (R), capacitance (C), and inductance (L) values. Other works were reported on different memristor-based memory devices [17–19], photonic memristor for neuromorphic computing [20], bioinspired memristors [21, 22], memristor-based biologically plausible memory [23], etc. In a recent study, Sangwan et al. reported a review on different nanomaterial-based memristive and ionic devices for application in neuromorphic computing architectures

[24]. Along with its electrical properties, density of memory element also affects the performance of the memristive device. Using core/shell nanoparticles instead of simple nanostructure, multilevel conductivity can be achieved which in turn would increase the density of memory elements [25].

MR, MC, and MI behavior of single and metal-doped CdSe nanocomposites under different doping environment has been investigated and reported by Das et al. in 2018 [26]. However, they used manganese (Mn) and copper (Cu) for doping and solubility of transient metal ions in CdSe is very low. Also doping can cause undesired structures and characterization alteration, which is not suitable for the devices. We propose a novel approach of core–shell nanoparticle-based devices to remove this problem. It is found that with suitable shell material, the mem-behavior of CdS quantum dots could be altered significantly. The present study emphasizes on the effect of ZnS and PbS shell on the mem-behavior of CdS quantum dots. Also, with change in molarity of the CdS core and ZnS and PbS shell, I–V characteristics of the nanocomposites were recorded and compared. Interesting hysteresis behavior is observed for the as-synthesized samples, and it is found that the inclusion of ZnS and PbS shell to the CdS core significantly alters its mem-behavior. The present study is also the first to report on mem-behavior of CdS@ZnS and CdS@PbS core–shell devices which provides a new prospect for further research in this domain.

2 Experimental

2.1 Synthesis of quantum dots/core–shell nanoparticles

Chemical route is used to synthesize CdS, CdS@ZnS, and CdS@PbS nanocomposites. Cadmium acetate $(Cd(CH_3COO)_2 \cdot 2H_2O, 99.99\%)$ and sodium sulphide $(Na_2S, 99.99\%)$ were purchased from Sigma and used without further purification. Polyvinylpyrrolidone (PVP) is used as capping material. Double distilled water is used as solvent for all the experiments. For synthesis of CdS@ZnS and CdS@PbS core–shell nanoparticles, Zinc Acetate $(Zn(CH_3COO)_2)$ and Lead(II) Nitrate $(Pb(NO_3)_2)$ is used as zinc and lead source, respectively. In a typical procedure, different concentrations of cadmium acetate and sodium sulphide solutions were prepared separately using de-

ionized water as solvent by keeping the Cd^{2+}:S^{2-} molar ratio at 1:1 and saturated with nitrogen gas for 1 h. This solution is than stirred for 2 h at 40 °C under nitrogen environment. Sodium sulphide is then added drop wise to this solution and further stirred for 3 h at 60 °C. The resultant bright yellow-colored CdS quantum dots were collected and kept overnight for stabilization. Epitaxial ZnS and PbS shell is grown separately on the as-synthesized CdS quantum dots (QDs) to form CdS@ZnS type-I and CdS@PbS type-II core–shell nanoparticles by keeping the concentration of shell precursor 10 times less compared to the core concentration [27]. For ZnS shell growth, zinc acetate and sodium sulphide solutions were prepared separately and added to the CdS core in the step of 1 ml alternately along with 3 wt% PVP solution under constant stirring. The solution is then constantly stirred for 5 h at 50 °C under continuous circulation of nitrogen gas. The resultant PVP-capped CdS@ZnS core–shell nanoparticles were collected. Similarly, PbS shell is also grown over CdS quantum dots. Aqua's solution of lead nitrate and sodium sulphide is prepared and added to the CdS core in step of 1 ml alternately along with 3 wt% PVP solution. The solution is then constantly stirred for 5 h at 50 °C under continuous circulation of nitrogen gas. The resultant PVP-capped CdS@PbS core–shell nanoparticles were collected afterward. All the samples were washed several times with distilled water and absolute alcohol to remove any impurity present. The resulting samples with different core and shell molarities along with their sample code are provided in Table 1.

2.2 Characterization

The X-ray diffraction (XRD) patterns of the as-synthesized samples were recorded using Phillips X'Pert Pro Powder X-ray Diffractometer ($\lambda = 1.54$ Å) and are shown in Fig. 1. The diffraction peaks obtained indicate a hexagonal structure for CdS quantum dots (JCPDS No. 41-1094), as shown in Fig. 1a. For CdS@ZnS and CdS@PbS core–shell samples, no independent peaks are observed for free ZnS and PbS particles, also the positions of the diffraction peaks are closer to the CdS core compared to ZnS and PbS shell, indicating that no alloy is formed and successful formation of high-quality CdS@ZnS and CdS@PbS core–shell nanoparticles. Broadening of the diffraction peaks are observed attributing to the

Table 1 Molarity, estimated band gap from UV–visible, and average particle size from XRD pattern

SL. no.	Sample code	Material (core/shell)	Molarity (mM)		Band gap from UV (eV)	Crystallite size form XRD (nm)
			Core	Shell		
1	S1	CdS	20	–	2.63	5.59
2	S2		30	–	2.68	–
3	S3		40	–	2.71	4.07
4	S4		50	–	2.72	3.76
5	S5		60	–	2.73	–
6	CZ1	CdS/ZnS	20	2	2.39	–
7	CZ2		30	3	2.42	–
8	CZ3		40	4	2.44	5.8
9	CZ4		50	5	2.47	14.3
10	CZ5		60	6	2.51	16.7
11	CP1	CdS/PbS	20	2	2.36	–
12	CP2		30	3	2.41	–
13	CP3		40	4	2.45	5.38
14	CP4		50	5	2.49	3.34
15	CP5		60	6	2.53	–

Fig. 1 X-ray diffraction pattern of **a** CdS (S1) and **b** CdS@ZnS (CZ3) and CdS@PbS (CP3) nanoparticles
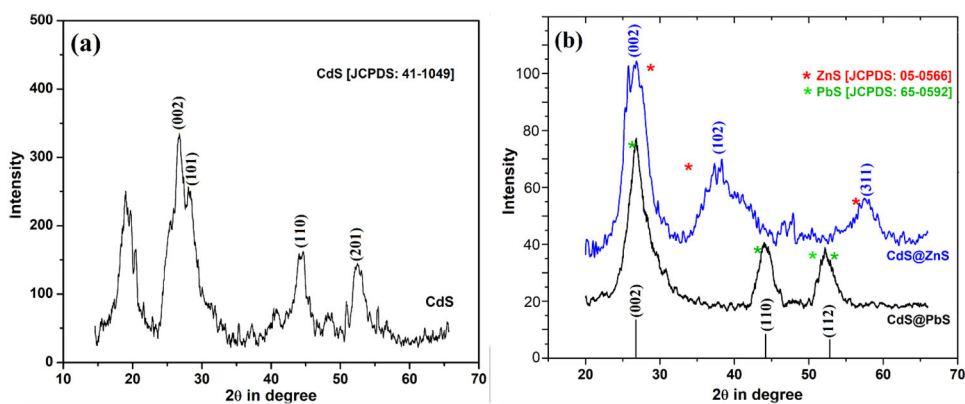
nanoformation of the samples. For CdS quantum dots, clear diffraction peaks are observed in (002), (101), (110), and (201) plans with (002) peak having the maximum intensity. In Fig. 1b, the diffraction peaks for CdS@ZnS nanoparticles can be observed in (002), (102), and (311) plans, and those for CdS@PbS nanoparicles peaks are observed in (002), (101), and (112) plans.

The average crystallite sizes of the samples are calculated using the Scherer's equation [28] and are given in Table 1.

The Ultraviolet–Visible (UV) and Photoluminescence (PL) spectroscopy of the as-synthesized samples are shown in Fig. 2a and b, respectively. The absorption edge for sample S1 is found to be around 465.2 nm which is much lower compared to the bulk

CdS absorption of 514 nm. This shift in absorption toward lower wavelengths is due to the quantum confinement effect indicating nanoformation of the as-synthesized samples. For the core–shell samples, absorption edge is found at 495.5 nm and 499.5 nm for CZ3 and CP3, respectively. The red shift in absorption of core–shell nanoparticles compared to CdS core is observed due to the increase in particle size after the growth of ZnS and PbS shell, respectively.

The PL spectra show a red shift from corresponding absorption values for the samples which may be due to the presence defects and trap states in the samples. For sample S1, low-energy PL peak with small stokes shift of ∼ 0.1 eV is observed, indicating that band-edge emission is dominant; however, the

Fig. 2 a UV–visible, and **b** PL spectroscopy of sample S1, CZ3, and CP3
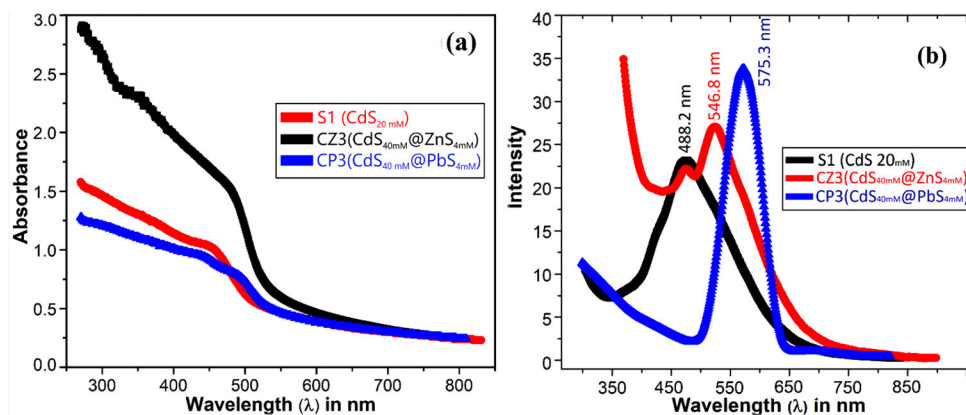
broad emission band with full width at half maximum (FWHM) of around ~ 65.2 nm suggests presence of possible overlapped defect-related emission, which is also supported by other studies [29]. For CdS@ZnS and CdS@PbS nanoparticles, the stokes shift increases to ~ 0.18 eV and 0.30 eV, respectively, compared to CdS core, indicating dominant trap state emission due to surface defects present within the band gap. Similar results are obtained by Liu et al. for CdS@ZnS core–shell nanoparticles [30]. The red-shifted PL spectra with broad emission band can be attributed to the broad size distribution of the nanocomposites and presence of multiple defect states at the nanocrystal surface [31, 32].

The band gap of the samples are estimated by the Tauc's equation [33] and are given in Table 1. It is observed that with the increase in morality, the band gap of the samples also increases which is also reported in other studies [34]. For core–shell samples, band gap is smaller compared to the core which is due to the fact that with the inclusion of shell, the size of the particle increases which in turn reduces the overall band gap. From XRD, it is observed that the sizes of CdS@ZnS core–shell nanoparticles are larger compared to CdS and CdS@PbS nanoparticles. Thus, from Table 1, it can be concluded that the observed blue shift in the absorption spectra and enhancement in the band gap is due to the quantum confinement and nanoformation of the samples.

High-resolution transmission electron microscopy (HRTEM) and selective area electron diffraction (SAED) images for samples S1, CZ3, and CP3 are recorded using JEM-2100 (200 kV, Jeol) and shown in Fig. 3a–c, respectively. The CdS quantum dots are found to be spherical in nature with particle sizes below ~ 10 nm. Agglomeration of the particles is

also observed which is quite common in colloidal matrix solution [35]. From Fig. 3b and c, formation of CdS@ZnS and CdS@PbS core–shell nanoparticles can be clearly seen with epitaxial growth of ZnS and PbS shell over CdS core. For CdS@ZnS nanoparticles, the average particle size is calculated around ~ 15 nm and shell thickness calculated for CZ3 is about 2 ± 2 nm, as shown in Fig. 3b. For CdS@PbS nanoparticles, particle size is found to be below 12 nm with shell thickness calculated around 5 ± 2 nm for CP3, as shown in Fig. 3c. The crystalline planes for CdS core, CdS@ZnS, and CdS@PbS core–shell nanoparticles can be seen in SAED images shown in Fig. 3 which are also seen in XRD measurements.

Atomic force microscopy is used to study the surface morphologies of the as-fabricated thin films for device applications. The AFM image of the prepared thin films with sample S1, CZ3, and CP3 in an area of ~ 140 nm $\times 140$ nm is shown in Fig. 4a–c, respectively. A large number of particles of different sizes forming a cluster of nanoparticles can be clearly seen in the pictures. It is also observed that the shape of the particles is nearly spherical. The prepared films have rough surface with the presence of hills and valleys. The film thickness can be estimated to have a value < 0.70 μm which is quite satisfactory for spin-coated films.

3 Results

3.1 Mem-behavior of the fabricated devices

To investigate the mem-behavior of the as-synthesized samples, simple devices are fabricated using ITO and Al as electrodes. A schematic diagram of the

Fig. 3 HRTEM and SAED images of **a** S1, **b** CZ3, and **c** CP3. **d** Schematic of the as-fabricated Core/Core@shell device
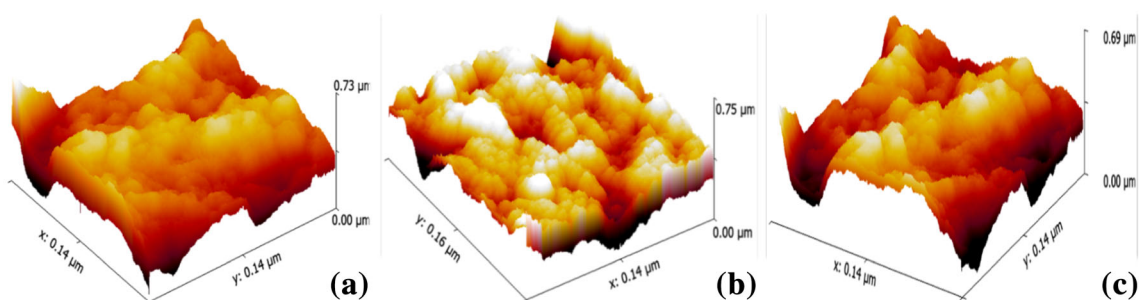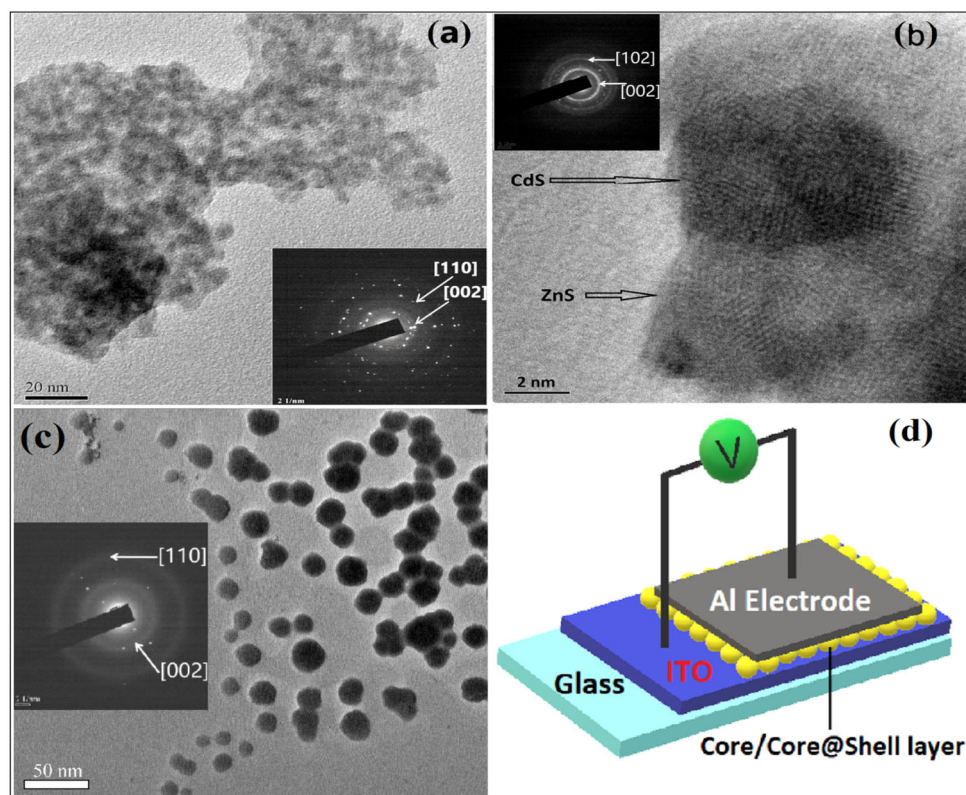

Fig. 4 AFM image of **a** S1, **b** CZ3, and **c** CP3, respectively

same is shown in Fig. 3d. Electrical characterizations are carried out for the as-fabricated quantum dots/core–shell nanoparticle devices using Keithley Source Meter (Model: 2450) and data are recorded using the kick start software. Initially, a layer of core/core–shell nanoparticle is deposited on an ITO-coated glass plate (resistivity $\sim 15\ \Omega$) using spin coating technique. Aluminium (Al) is then used as a counter electrode and deposited over the ITO-coated film consisting of the nanocomposites using thermal evaporation technique. Similar devices are fabricated with all other synthesized samples and the corresponding current–voltage (I–V) characteristics are recorded at room temperature.

Figure 5a and b shows the hysteresis behavior of the as-fabricated ITO/CdS(S1)/Al quantum dot device at room temperature. The current–voltage readings were taken inside an insulated box made from PVC material to prevent any external disturbance. A swapping voltage from $(- V) \rightarrow (+ V) \rightarrow (- V)$ is applied from a Keithley source meter and the corresponding current values are recorded. Both forward $[(- V) \rightarrow (+ V)]$ and reverse $[(+ V) \rightarrow (- V)]$ paths having different amplitudes in currents for the same voltages with prominent hysteresis behavior are observed. Similarly, for other CdS quantum dot samples (i.e., S2, S3, S4, and S5), devices were fabricated with ITO and Al as
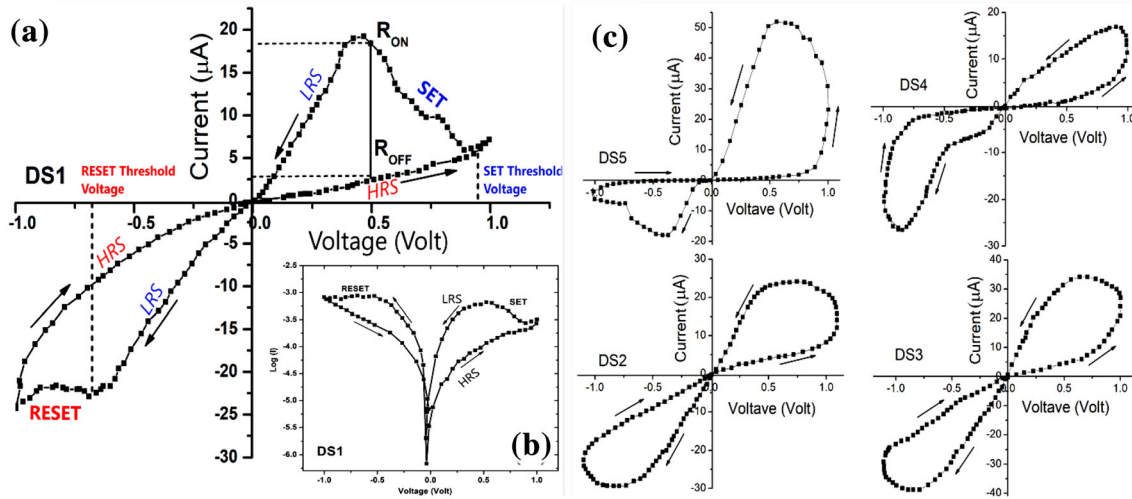
Fig. 5 **a** I–V characteristics of ITO/S1/Al quantum dot-based memristive device, **b** Log(I)–V characteristics in the logarithmic scale at room temperature, and **c** I–V characteristics of DS2-DS5

electrodes and the corresponding I–V characteristics are recorded and shown in Fig. 5c. The ratio of ON and OFF resistance (R_{ON}/R_{OFF}) of the device, which is also known as the memristor efficiency factor (MEF), is calculated from the I–V characteristics curve, as shown in Fig. 5a. This R_{ON}/R_{OFF} ratio (loop area) determines the sensitivity of the devices [36]. A larger ratio indicates high sensing capability and vice versa. A higher value of R_{ON}/R_{OFF} ratio (> 10) enhances the efficiency of the memory devices. The device codes for all the as-fabricated devices with calculated R_{ON}/R_{OFF} values and other measured parameters are given in Table 2. The presence of pinched hysteresis loops in the I–V characteristics curve indicates that the devices exhibit bipolar switching properties. Initially, the device is at high resistance state (OFF state) when no external bias is applied and switches to low resistance state (ON state) under the influence of sufficient voltage or current pulse across its terminals. This applied potential (V_{SET}) creates a conducting path in the active layer consisting of the quantum dots/core–shell nanoparticles and switch the memristor from HRS to LRS (SET operation). Similarly, for reset operation (LRS to HRS), a threshold voltage (V_{RESET}) is applied, as shown in Fig. 5a. When the applied voltage is initially swept from 0 to + 1 V at room temperature, the device changes its state from HRS to LRS (SET operation) which can be considered to logic '1' operation. For reset operation, a voltage of − 1 V to + 1 V is applied across the device which changes

its resistance from LRS to HRS (RESET operation) and logic '0' is written into the cell. Figure 5b represents the I–V characteristics of the device in the logarithmic scale.

For all the ITO/CdS QDs/Al nanoscale devices (DS1, DS2, DS3, DS4, and DS5), bipolar memristive behavior is observed with a variation in R_{ON}/R_{OFF} ratio as well as slight variation in the V_{SET} and V_{RESET} voltages. It is observed that the R_{ON}/R_{OFF} ratio increases for the devices with higher quantum dot concentration (sample molarity) in the active layer as it increases the filling fraction of the active layer [37]. The SET (V_{SET}) and RESET (V_{RESET}) threshold voltages recorded for all the ITO/CdS QDs/Al devices are found in the range of 0.91–1.06 V and − 0.41 V to 0.88 V, respectively (Table 2). The list variations in V_{SET} and V_{RESET} (except device DS1 and DS5) threshold voltages of the fabricated devices make them suitable candidates for possible application in high-density memory array formation. Figure 6 shows the I–V characteristics of ITO/CdS@ZnS NPs/Al and ITO/CdS@PbS NPs/Al devices. For device DC1–DC5 (CdS@ZnS core–shell devices), nonzero crossing of the I–V curve is observed with memcapacitive (MC) behavior at room temperature indicating retention of charges at 0 V, as shown in Fig. 6a. This extended memristive behavior could be understood by studies which shows that at nanoscale, capacitive behavior is always present in memristive systems to some extent [38].

Table 2 Different measured parameters and device codes of the as-synthesized samples

Serial no.	Device construction	Device code	R_{ON}/R_{OFF} ratio	Threshold voltage		Observed device mem-behavior
				V_{SET} (Volt)	V_{RESET} (Volt)	
01	ITO/S1/Al	DS1	2.54	0.97	− 0.51	MR
02	ITO/S2/Al	DS2	4.87	1.06	− 0.88	MR
03	ITO/S3/Al	DS3	5.65	0.99	− 0.85	MR
04	ITO/S4/Al	DS4	4.13	0.99	− 0.84	MR
05	ITO/S5/Al	DS5	25.23	0.91	− 0.41	MR
06	ITO/CZ1/Al	DC1	4.61	0.98	− 0.90	MC
07	ITO/CZ2/Al	DC2	3.10	1.07	− 0.18	MC
08	ITO/CZ3/Al	DC3	8.40	0.98	− 0.61	MC
09	ITO/CZ4/Al	DC4	5.35	1.00	− 0.89	MC
10	ITO/CZ5/Al	DC5	28.57	0.99	− 0.56	MC
11	ITO/CP1/Al	DC6	1.13	0.99	− 0.99	MI
12	ITO/CP2/Al	DC7	1.25	0.98	− 0.92	MI
13	ITO/CP3/Al	DC8	1.96	1.07	− 1.06	MI
14	ITO/CP4/Al	DC9	1.51	0.95	− 0.97	MI
15	ITO/CP5/Al	DC10	1.69	0.98	− 0.96	MI

Fig. 6 Bipolar hysteresis behavior of **a** ITO/CdS@ZnS NPs/Al (DC1–DC5) devices and **b** ITO/CdS@ZnS NPs/Al (DC6–DC10) devices
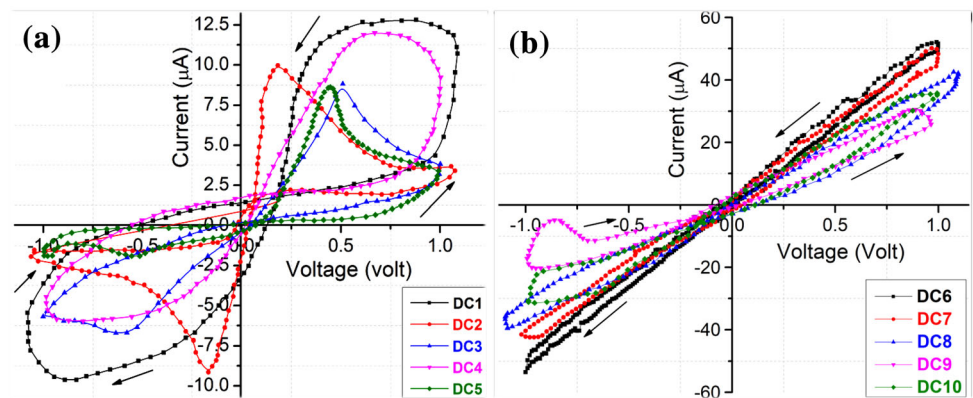
The nanoparticles and the capping material (PVP) form a repeating conducting and insulating region in the active layer which gives rise to the time-dependent capacitance (C_t) in addition to the time-dependent resistance (R_t) [9]. The R_{ON}/R_{OFF} ratios for CdS@ZnS core–shell devices (DC1–DC5) are found to be higher (except DC2) compared to CdS core quantum dot devices. It may be due to the addition of higher band-gap ZnS shell which enhances the energy levels for LUMO in the CdS@ZnS nanoparticles. Figure 6b shows the mem-behavior of the CdS@PbS core–shell devices (DC6–DC10) at room temperature. The recorded I–V characteristics show bipolar hysteresis properties with pinching in the third quadrant, indicating that the behavior is meminductive (MI) in nature. For all the CdS@PbS nanoparticle devices, meminductive behavior is observed with a narrow loop area (small R_{ON}/R_{OFF} ratio) ranges from 1.23 to 1.96. Thus, an interesting change in the mem-behavior of the CdS quantum dot device is observed with the change of shell material. With a large band-gap shell material, CdS@ZnS type-II core–shell nanoparticle devices exhibits memcapacitive behavior, whereas with a lower band gap shell, CdS@PbS type-I core–shell nanoparticle devices show hysteresis properties which is meminductive in nature. These variations in mem-behavior/parameters of the fabricated devices could be due to different shell materials and molarity of the core and shell

which calls for further theoretical and experimental study.

The *I–V* characteristics of the CdS, CdS@ZnS, and CdS@PbS quantum dot devices in logarithmic scale are shown in Fig. 7a–c, respectively. The hysteresis width at '0 V' (HWO) is calculated for all the devices and plotted as a function of sample molarity, as shown in Fig. 7d. For all the devices (except DS5), the HWO is found to be an increasing function with the increase in molarity.

The conduction of current through the active layer consisting of quantum dots/core–shell nanoparticles separated by a dielectric capping material (PVP) could be either coulomb blockade (CB) or resonant tunneling (RT) in nature. From the *I–V* characteristics of the fabricated devices, it is evident that no negative differential resistance (NDR) region is present, and hence, RT can be ruled out. The ON/OFF switching mechanism of the *I–V* characteristics is also supported by the coulomb blockade on the basis of the trapping of charge in the nanoparticles. As the nanoparticle is excited by an electron the tunneling through it is opposed by the coulomb charging energy. The trapped charges form space charge, and it lowers the external electric field due to induced

internal electric field and further opposes any flow of charge carriers. Thus, the device undergoes a transition from LRS to HRS.
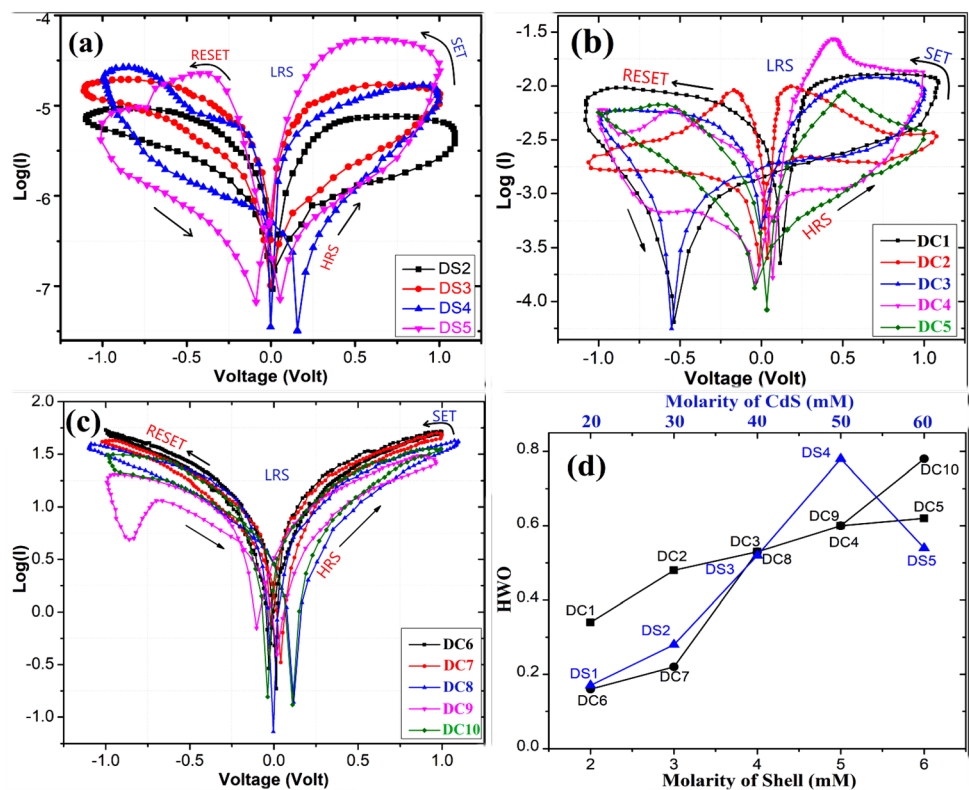
By reversing the voltages at the two terminals, the trapped charges can be released, and as a result, the device makes a transition from HRS to LRS. The asymmetry of the *I–V* characteristics is due to the Schottky controlled conduction of the device which can be confirmed by the I–$V^{1/2}$ graph, as shown in Fig. 8a and b. The following equation can be used to describe the current through the device in terms of a state variable ω which is defined as the area covered by the conducting channel [39]:

$$I = \omega\gamma\sinh(\delta \times V) + (1 - \omega)\alpha\left(1 - e^{-\beta \times V}\right). \quad (1)$$

Here, γ = effective tunneling distance, δ = tunneling barrier, and α = depletion width of the Schottky barrier region and β = Schottky barrier height.

The first term of Eq. (1) represents the conduction of current through the channel region and the second term represents the conduction through the rest of the device which is Schottky dominated conduction [40]. This equation is regulated by the state variable ω and positive parameters γ, δ, α, and β. The memristor efficiency factor (R_{ON}/R_{OFF}) as a function of molarity

Fig. 7 Switching behavior of the as-fabricated devices in logarithmic scale: **a** ITO/CdS QDs/Al devices (DS2–DS5), **b** ITO/CdS@ZnS NPs/Al devices (DC1–DC5), and **c** ITO/CdS@PbS NPs/Al devices (DC6–DC10). **d** Variation of HWO with respect to the molarity of the devices. Blue line is for CdS core devices and black lines for CdS@ZnS and CdS@PbS core–shell devices
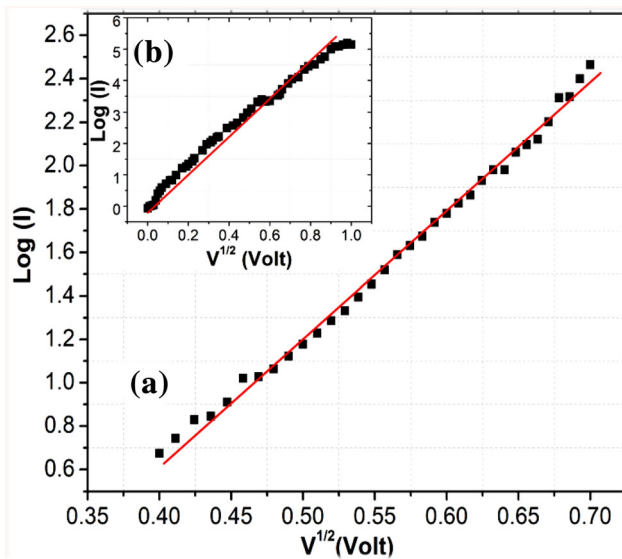
Fig. 8 Log(I)–$V^{1/2}$ graph at **a** HRS and **b** LRS region

4 Discussion

The recorded current–voltage characteristics of the fabricated devices show bipolar resistive switching properties with presence of prominent hysteresis loops. The present study is the first to introduce the idea of controlling the mem-behavior of CdS quantum dot devices by adding ZnS and PbS epitaxial shell which is also verified by our experimental results. For CdS@ZnS core–shell devices, nonzero crossing of I–V curve is observed with pinching in the first quadrant and thus showing MC behavior. The addition of ZnS shell changes the overall capacitance of the nanoparticles system which could affect the electrical properties of the devices. It is also observed that by simply changing the molarity of the shell, device parameters such as R_{ON}/R_{OFF}, V_{SET}, V_{RESET}, device maximum current, etc. could be controlled. For CdS@PbS core–shell devices, MI behavior is observed. These findings, however, call for further theoretical and experimental study. The value of set threshold voltage (V_{SET}) for all the devices ranges from 0.91 to 1.07 V with a deviation of 0.16 V only. However, for V_{RESET}, some deviations are observed in CdS core and CdS@ZnS core–shell devices. For CdS@PbS devices, value of V_{RESET} ranges from 0.92 to 1.06 V with a variation of 0.14 V only. The R_{ON}/R_{OFF} ratio is found to have a positive correlation with the molarity of the samples. It is found to be maximum for device DC5 ($\sim$ 28.57) and minimum for DC6 ($\sim$ 1.23). It is also observed that CdS@PbS core–shell nanoparticle devices have the lowest R_{ON}/R_{OFF} ratio, and hence, it will have a poor sensitivity.

5 Conclusion

Syntheses of CdS, CdS@ZnS, and CdS@PbS nanoparticles are done using PVP as capping material adopting chemical route. Different characterization techniques such as XRD, UV–visible, and PL spectroscopy, HRTEM & SAED, and AFM are used to confirm the nanoformation of the samples. The as-synthesized samples are used to fabricate devices to study their mem-behavior. The recorded I–V characteristics of the devices show MR behavior for CdS quantum dot devices and MC and MI behavior for CdS@ZnS and CdS@PbS core–shell devices, respectively. The main challenge for nanomaterial-based memory devices is the variation of the device

of the samples is plotted in Fig. 9. It can be observed from the graph that CdS@ZnS core–shell devices have a higher efficiency (except device DC2) compared to the CdS core quantum dot devices (DS1–DS5). However, the CdS@PbS core–shell devices show the lowest efficiency factor (R_{ON}/R_{OFF}).

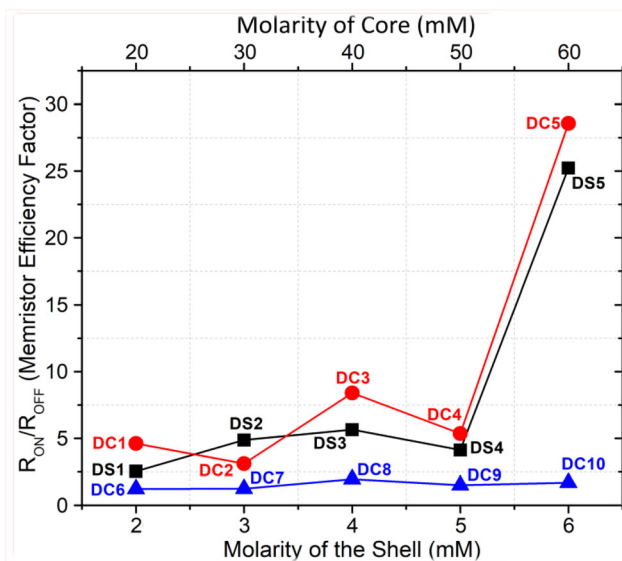**Fig. 9** R_{ON}/R_{OFF} graph as a function of molarity

parameters (R_{ON}/R_{OFF}, V_{SET}, and V_{RESET}) which makes it difficult to fabricate memory arrays. From the present investigation, CdS@PbS core–shell devices show best stability in terms of SET/RESET threshold voltages; however, it has the lowest R_{ON}/R_{OFF} ratio indicating poor memory efficiency. The CdS@ZnS core–shell devices show that the best R_{ON}/R_{OFF} ratios and higher efficiency with V_{SET} values are found to have very small variations with the change in molarity. However, V_{RESET} values show some nonlinearity and need further improvements. It is evident from the present study that the addition of ZnS and PbS shell significantly alters the mem-behavior of CdS quantum dots which can be used to design desired MC and MI devices for various potential applications. The current findings could act as a base for future study of this nanomaterial-based devices for further improvements in their performance by controlling the device parameters and different material properties.

Acknowledgements

Author contributions

All the experimental and theoretical works are done by 'HD'. The paper is written by 'HD' and helped by 'QX'. Technical guidance was provided by 'QX' and also some necessary modifications are done by him. This whole work is guided by 'PD' and theoretical concepts were introduced in the paper by her. All the three authors finally checked and approved the manuscript.

Funding

Data availability

The datasets used and/or analysed during the current study are available from the corresponding author on reasonable request.

Compliance with ethical standards

Conflict of interest The authors declare that they have no competing interests in this section.

References

1. L.O. Chua, IEEE Trans. Circuit Theory **18**, 507 (1971)
2. D.B. Strukov, G.S. Snider, D.R. Stewart, R.S. Williams, Nature **453**, 80 (2008)
3. A. Priyadharsan, S. Shanavas, C. Vidya, J. Kalyana Sundar, R. Acevedo, P.M. Anbarasan, Mater. Today **26**, 3522–3525 (2019)
4. F. Flory, L. Escoubas, G. Berginc, J. of Nanophotonics **5**(1), 052502 (2011)
5. P. Christian, F. Von der Kammer, M. Baalousha, T. Hofmann, Ecotoxicology **17**(5), 326–343 (2008)
6. E.S. Kannan, G.H. Kim, D.A. Ritchie, J. Phys. D **43**, 225101 (2010)
7. M. Russ, A. Lorke, D. Reuter, P. Schafmeister, Physica E **22**, 506 (2004)
8. H. Das, P. Datta, J. Exp, Nanoscience **11**(11), 901–915 (2016)
9. T.H. Kim, E.Y. Jang, N.J. Lee, D.J. Choi, K.-J. Lee, J.-T. Jang, J.-S. Choi, S.H. Moon, J. Cheon, Nano Lett. **9**, 2229–2233 (2009)
10. R. Bhadra, P. Datta, K.C. Sharma, J. Dispers. Sci. Technol. **29**(8), 1138–1142 (2008)
11. S. Sarma, B.M. Mothudi, M.S. Dhlamini, J. Mater. Sci. **27**, 4551–4558 (2016)
12. P. Cheng, K. Sun, Y.H. Hu, Nano Lett. **16**, 572–576 (2016)
13. S. Chakrabarti, A.J. Pal, Nanoscale **7**, 9886–9893 (2015)
14. Y.C. Yang, F. Pan, Q. Liu, M. Liu, F. Zeng, Nano Lett. **9**, 1636 (2009)
15. A. Younis, D. Chu, Xi. Lin, J. Yi, F. Dang, S. Li, ACS Appl. Mater. Interfaces **5**, 2249–2254 (2013)
16. J. Devi, B. Das, S. Sarma, P. Datta, Indian J. Phys. **92**, 1541–1550 (2018)
17. L.Q. Jiang, A. Khiat, I. Salaoru, C. Papavassiliou, X. Hui, T. Prodromakis, Sci. Rep. **4**, 4522 (2014)
18. Do Hyeong Kim, Chaoxing Wu, Dong Hyun Park, Woo Kyum Kim, Hae WoonSeo, Sang Wook Kim and Tae Whan Kim. ACS Appl. Mater. Interfaces **10**(17), 14843–14849 (2018)

19. J. Guo, S. Guo, X. Su, S. Zhu, Y. Pang, W. Luo, J. Zhang, H. Sun, H. Li, D. Zhang, ACS Appl Electron. Mater **2**(3), 817–837 (2020)

20. F. Alibart, L. Gao, B.D. Hoskins, D.B. Strukov, Nanotechnology **23**, 075201 (2012)

21. E. Goi, Q. Zhang, Xi. Chen, H. Luan, Gu. Min, PhotoniX **1**, 3 (2020)

22. Fu. Tianda, X. Liu, H. Gao, J.E. Ward, X. Liu et al., Nat. Commun. **11**, 1861 (2020)

23. Y. Hiruma, K. Yoshikawa, M.-A. Haga, Faraday Discuss **213**, 99–113 (2019)

24. V.K. Sangwan, M.C. Hersam, Nat. Nanotechnol. **15**, 517–528 (2020)

25. Y. Wang, Yu. Liutao, Wu. Si, Ru. Huang, Y. Yang, Adv. Intell. Syst. **2**, 2000001 (2020)

26. B. Das, J. Devi, P.K. Kalita, P. Datta, J. Mater. Sci. **29**, 546–557 (2018)

27. D. Das, A.M.P. Hussain, Appl. Phys. A **125**, 826 (2019)

28. P. Scherrer, Göttinger Nachrichten Gesell. **2**, 98 (1918)

29. J. Joo, H.B. Na, T. Yu, J.H. Yu et al., J. Am. Chem. Soc. **125**(36), 11100–11105 (2003)

30. L.-W. Liu, S.-Y. Hu, Y. Pan, J.Q. Zhang et al., Beilstein J. Nanotechnol. **5**, 919–926 (2014)

31. J. Mooney, M.M. Krause, J.I. Saari, P. Kambhampati, J. Chem. Phys. **138**, 204705 (2013)

32. D.R. Baker, P.V. Kamat, Langmuir **26**, 11272 (2010)

33. J. Tauc, Mater. Res. Bull. **3**(1), 37–46 (1968)

34. S.D. Birajdar, A.B. Shinde, G.B. Kadam, P.M. Kshirsagar, M.N. Sarnaik, IJARBAS **2**(1), 74–77 (2015)

35. P.K. Kalita, B. Das, R. Devi, J. Pure Appl. Chem. **4**, 97–107 (2014)

36. N.S.M. Hadisa, A.A. Manafa, S.H. Ngalimc, S.H. Hermand, Sens Bio Sens Res **14**, 21–29 (2017)

37. D.Y. Yun, T.W. Kim, S.W. Kim, Thin Solid Films **544**, 433–436 (2013)

38. M.D. Ventra, Y.V. Pershin, L.O. Chua, Proc. IEEE **9**, 1717 (2009)

39. S. Choi, P. Sheridan, W.D. Lu, Data Sci. Rep. **5**, 10492 (2015)

40. T. Chang, S.H. Jo, K.-H. Ki, P. Sheridan, S. Gaba, W. Lu, Appl. Phys. A **102**, 857–863 (2011)